Evaluation of high-quality image reconstruction techniques applied to high-resolution Z-contrast imaging

G. Bárcena-González[a,*], M. P. Guerrero-Lebrero[a], E. Guerrero[a], A. Yañez[a], D. Fernández-Reyes[b], D. González[b], P. L. Galindo[a]

[a]Department of Computer Science and Engineering, University of Cádiz, Spain

[b]Department of Material Science and Metallurgy Engineering and Inorganic Chemistry, University of Cádiz, Spain

Corresponding author: guillermo.barcena@uca.es

Abstract

High-quality image reconstruction techniques allow the generation of high pixel density images from a set of low-resolution micrographs. In general, these techniques consist of two main steps, namely, accurate registration, and formulation of an appropriate forward image model via some restoration method. There exist a wide variety of algorithms to cope with both stages and depending on their practical applications, some methods can outperform others, since they can be sensitive to the assumed data model, noise, drift, etc. When dealing with images generated by Z-contrast scanning transmission electron microscopes, a current trend is based on non-rigid approximations in the registration stage. In our work we aimed at reaching similar accuracy but addressing the most complex calculations in the reconstruction stage, instead of in the registration stage (as the non-rigid approaches do), but using a much smaller number of images. We review some of the most significant methods and address their shortcomings when they are applied to the field of microscopy. Simulated images with known targets will be used to evaluate and compare the main approaches in terms of quality enhancement and computing time. In addition, a procedure to determine the reference image will be proposed to minimise the global drift on the series. The best registration and restoration strategies will be applied to experimental images in order to point up the enhanced capability of this high quality image reconstruction methodology in this field.

Keywords: High quality image reconstruction, registration, restoration, Z-contrast images

1. Introduction

High-resolution Z-contrast Scanning Transmission Electron Microscopy (HRSTEM) provides images of crystals at atomic resolution, where the location

of atom column positions is greatly simplified [1]. In particular, when using a High Angle Annular Dark Field (HAADF) detector, the intensity of atom columns approximately reflects their mean square atomic number (Z) [2]. Although transmission electron microscopy has reached unprecedented resolution, with values that are ranging from 65 thousand pixels per image (256x256) to 64 million (8192x8192), some artefacts and distortions can appear in the final image. Mainly they are caused by different perturbations such as airflow, acoustic noise, floor vibrations or fluctuations in AC and DC magnetic fields and temperature during the image acquisition process. Thus, not only the resolution limit of the microscope but also this presence of noise, drift and distortions can compromise the level of detail.

The process of taking a sequence of under-sampled Low Resolution (LR) images of a particular scene and generating a High Resolution (HR) image, providing far more detail and quality than any individual LR image is known as Super-Resolution (SR) image reconstruction in standard Image Processing [3], [4]. However in the Microscopy context Super-Resolution is a form of light microscopy that allows images to be taken with a higher resolution than the diffraction limit [5], then we have renamed the Image Processing concept of SR as High Quality Image Reconstruction (HQIR). Regardless of the name used, this technique can provide a final more detailed image overcoming the inherent resolution limitation of the microscope.

In general, HQIR methodology comprises two stages: registration and reconstruction. In the registration process LR images need to be mapped into a common reference frame and that can be made in two ways. Some authors, as Yankovich [6] or Berkels [7],[8] use non-rigid registration with a variational approach that transforms two frames into a common coordinate system with a nonparametric transformation, in order to reduce the displacements of the imaged atoms that are produced by the serial acquisition process in STEM imaging. Our goal is to reach the same objective but using rigid alignment and fixing the displacements in the reconstruction stage, where information from different images is combined into a single high-resolution micrograph with more definition and quality [4]. Furthermore, we use a number of images considerably smaller than non-rigid proposals. Nowadays, there exist a wide variety of HQIR methods to cope with the registration and restoration stages; however, the development of an ultimate methodology for HQIR can be driven by the use to which the super-resolved image is put.

Thus, sections 2 and 3 have been devoted to review the algorithms for registration and reconstruction that have been used in this comparative study. Section 4 describes the simulation procedure to obtain the target images and different sets of shifted and rotated images degraded by noise from these targets. Metrics to compare these strategies have also been detailed. Section 5 presents the results of the different rigid alignment and restoration methods and the most suitable algorithms are selected. In section 6, they are applied to an

experimental image where we illustrate how HQIR techniques can be used to enhance HAADF images.

2. Image Registration Algorithms

Image registration involves the geometrical (rotation, translation, shearing, scale, …) alignment of images where one of them is used as reference. Image registration is a crucial step in all image analysis tasks in which the final information is gained from the combination of various data sources [9].
Image registration methods can be classified into Non-rigid and Rigid approaches. Currently, some authors use non-rigid alignment in order to determine possible irregularities in the atomic structure achieving sub-picometre precision [6]–[8],[10]. In contrast, here we use a small number of images and we focus on the assessment of rigid alignment methods, together with a more complex restoration stage.
Because the number of rigid registration algorithms is too high, in this paper different techniques have been selected based on their potential applications on the field of microscopy. Three of the selected methods (Marcel's [11], Lucchese's [12], Vandewalle's [13]), fall into the frequency domain category while Keren's approach [14] belongs to the spatial domain. In addition, we propose a variant of Vandewalle's approach to improve the accuracy of the registration using normalized cross-correlation.
Frequency domain HQIR methods provide the advantages of theoretical simplicity and low computational complexity, as well as they are highly amenable to parallel implementation due to the decoupling of the frequency domain equations[15]. Most approaches are based on the Fourier Shift Theorem: a shift in the spatial domain corresponds to a phase shift in the frequency domain, such as the widely used method presented by Marcel et al. [11] to estimate the translation between two images. These authors also proposed the use of log-polar coordinate changes to estimate rotation and scale changes. Lucchese and Cortelazzo [12] modified this proposal using a three-stage coarsest to finest procedure for rotation angle estimation with a wide range of accuracy degree, while the shift is estimated using a standard phase correlation calculation. Vandewalle et al. [13] presented another frequency domain technique to register a set of aliased images using low-frequency information: this part of the signal corresponds to the aliasing-free part of the images, having the highest signal-to-noise ratio (SNR). The phase difference between the compared images is computed, the corresponding system of linear equations for the aliasing-free frequencies is formed and the optimal shift parameters result from its least squares solution.
The original Vandewalle approach uses the differences of amplitudes in the Fourier transform seeking the maximum correlation for the calculation of the rotation angle. To do this, it defines the precision in degrees that will have the rotation angle between the images by converting the Fourier transform to polar

form. Subsequently the low frequency values are discarded and rectangular windows are traced over the Fourier transform being the window size equal to the precision angle. The profile from the average of the amplitude values is correlated to the reference image. This correlation determines the rotation angle between both images with high accuracy and it is very noise resistant. In this work, we also introduce a variant of this registration approach by combining Vandewalle's rotation angle calculations together with a similar procedure based on normalized cross correlation (NCC) to calculate the shift. The NCC of a series of images A regarding the reference image B is defined as:

$$\mathrm{NCC}=\frac{1}{\mathrm{NxM}}\sum_{i=1}^{N}\sum_{j=1}^{M}\frac{[A_{i,j}-\bar{A}]\ \ [B_{i,j}-\bar{B}]}{\sigma_A\sigma_B} \quad (1)$$

being $A_{i,j}$ ($B_{i,j}$) their intensity values at the position i,j where N and M are the number of rows and columns of the image A (B). $\bar{A}$ ($\bar{B}$) is the average and σ_A (σ_B) the standard deviation of all the intensity values in A (B).

On the other hand, spatial domain methods allow for more general motion models. Some typical criteria for intensity-based registration are the minimization of the squared error between the compared images, the correlation maximization [13] and the maximization of mutual information [16]. The accuracy of these methods depends highly on the performance of the interpolation algorithms. In this work, the proposal of Keren et al. will be compared against frequency domain methods. This spatial domain approach uses a Taylor's series expansion to represent shifts and global rotations between two images, and then they applied a Gaussian pyramidal scheme to increase the precision for large motion parameters.

2.1. Selecting the reference image

Even in the best cases, a certain drift effect (shift, shear or rotational) can occur that influences the overall image acquisition process. If the sample moves in the xy plane perpendicular to the optical axis, the image of the series undergoes a corresponding positional displacement on the image sensor. Additionally, each image of the series could suffer of non-linear displacements, such as flags (the pixel rows are shifted horizontally) and/or skips (the pixel rows are convoluted to neighbouring rows). While most of the registration applications use as reference the first image from the raw series, we hold that the reference image should be carefully selected in order to minimise i) the global drift on the series and ii) the presence of skips and flags. If an image of the series were randomly taken as reference, there would exist a high risk i) to loose information in the opposite direction to the drift, resulting in a final image after the registration process with less useful pixels in that direction or ii) to select an image with a high density of scanning errors.

Thus, we propose the following algorithm to select the best reference image (to minimise the drift effect) working with a low-pass filtered series of low-resolution images (see table 1). The application of a low-pass filtering permits that the shift can be easily calculated overcoming the presence of (partial) aliasing [13]. The resulting motion parameters obtained with respect to this reference image are applied to the original series, without filtering. In the following, for the different image registration methodologies, this algorithm will be used to select the reference image.

Table. 1. Algorithm to obtain the reference image and the motion parameters

1. Generate a low-pass filtered series from the set of the original LR *n* images
2. Take at random an image from the series of *n* low-pass filtered images to be the first reference
3. Repeat the following process:
   3.1. The reference image is located at first position in the series of images.
   3.2. Calculate shift and rotation parameters between two adjacent images. For *i*=2 to *n,* we calculate s_i, as the shift and rotation between image *i* and the previous one, *i-1*, (we use our proposal based on normalized cross-correlation and the application Vandewalle algorithm):

$$s_i = \text{shift \& rotation}(s_i, s_{i-1})$$

   3.3. Calculate total shift and rotation of a given image *i*, Ts_i, be defined as the sum of the shifts and rotations between two adjacent images calculated in step 2, for all the images from first to *i*-th position:

$$Ts_i = s_1 + \ldots + s_i$$

   3.4. Calculate the mean of the total shift and rotation values:

$$mTs = \text{mean}\,(Ts_i) \quad (i=1..n)$$

   3.5. Calculate the Euclidean distances from each total shift and rotation to the mean value:

$$D_i = \text{EuclideanDistance}(TS_i, mTs)$$

   3.6. Calculate D_{min}, as the minimum Euclidean distance, and keep the index i.

$$D_{min} = \text{Min}\,(D_i)$$

   3.7. if D_{min} is lower than its previous value, go back to step 3 taking image *i* as the new reference image.
4. Calculate shift and rotation parameters for each image from the low-pass filtered series with respect to the resulting reference image.
5. Finally, these motion parameters are applied to the series of images without filtering.

3. Restoration algorithms

In all HQIF restoration methods, an improved resolution image is generated from several low-resolution aligned images. Generally, HQIR restoration approaches in frequency domain have developed slowly since they lack ability to take the information in time-domain to frequency-domain [17]. To overcome these limitations many spatial domain approaches have been proposed.

At the simplest level, the value of a function between known samples could be estimated by taking the value of the nearest sample (nearest neighbour) or by using a weighted average of two/four translated neighbour pixels, so in our experiments we have been applied linear (LI) and bicubic (BI) interpolations [18]. Another approach proposed by Stark and Oskoui [19] used a projection onto convex set (POCS) algorithm to reconstruct the high-resolution image. This method was later extended by Tekalp et al. [20] to include noise. POCS defines a set of restrictions to limit the space of possible solutions for the inexistent pixels in the reconstruction. These limitations are defined as a convex set containing all the potential solutions. The goal of POCS approach is to find a vector that is in the intersection of convex sets. In each step of the iterative algorithm, an orthogonal projection is performed onto one of the convex sets. Bregman [21] showed that successive orthogonal projections converge to a vector that is in the intersection of all the convex sets. As a special case of POCS technique, Papoulis-Gerchberg method (PG) [22], [23] assumed that in the high-resolution image some of the pixel values are known and that the high frequency components are zero. The method tries to interpolate the unknown values and correct the aliasing for low frequency components. Furthermore, it does predict some of the high frequency values by forcing the known values.

Iterated Back Projection (IBP) [24] procedure is another method that updates the estimate of the HQIR reconstruction by backprojecting the error between the images obtained in the j-th iteration and the reference. A faster algorithm than IBP is Robust Super Resolution (RSR) suggested by Farsiu [18]. This algorithm first scale up the LR images and then, fuses all these LR images by a median filter to obtain the HR image. Finally, an optional deblurring kernel may be applied.

Non-Local Means (NLM) denoising algorithm was proposed by Buades et al. [25] and Protter et al. [26] adapted the method for HQIR purposes showing a very robust behaviour against inaccuracies in registration and motion tracking. NLM assumes that image content is likely to repeat itself within some neighbourhood; therefore, the algorithm calculates a weighted averaging on those pixels in the same patch (search window) whose intensity distributions are close to each other, in terms of the Euclidean distance. This algorithm is governed by three parameters, namely the weight-decay control parameter to manage the amount of noise to be taken into account in the final image, the

radius of the neighbourhood to find the similarity between two pixels and the radius of a search window, which is centred at the current pixel being computed. Binev et al. [27] proposed an alternative strategy more robust against outliers using the NLM-median but in this version, the target value is calculated by computing medians of source pixel values.
Anyway, reconstruction methods can be addressed either by maintaining the same number of pixels or by increasing the number of pixels per unit area. First approaches fall into the category of typical restoration algorithms while HQIR algorithms are specifically focused on increasing this number of pixels per unit area [28]. This paper deals with this last approach.

4. Materials & Methods

Simulated images of monocrystalline InP are generated and used as initial targets. On these images, we first apply different noise levels, followed by some other degradations as shifts and rotations and finally downsampled to obtain various series of LR frames. The aim is to apply the HQIR methodology to these series of LR frames. The resulting HQIR images will be compared against the initial targets in order to assess the performance of the above registration and restoration approaches when they are applied to HAADF-STEM images at different noise levels.
A supercell of InP containing all the information about atom position, composition, site occupancy and Debye-Waller factors is generated. This model together with the microscope parameters constitute the input to the SICSTEM program [29]. This parallel software can afford HAADF-STEM image simulations of nanostructures composed of several hundred thousand atoms following a multislice schema. Considering a 100 kV dedicated VG Microscope HB501UX STEM, an image of 1024 x 1024 pixels and oriented along the [110] direction is generated (fig. 1).

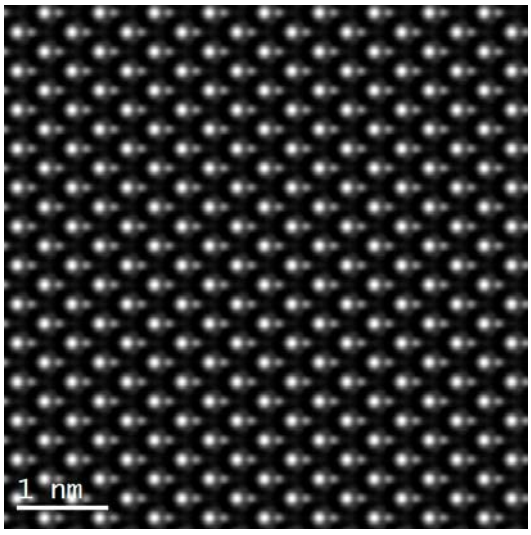

Fig.1. Simulated image generated by SICSTEM software from an InP supercell

Poisson noise, inherent in experimental micrographs, is modelled by a Normal distribution, and added to this simulated image. In this work, we have made 3 high resolution target images using different Gaussian distributions, namely σ=0.005, 0.01 and 0.02, (where σ is the standard deviation) in order to compare the effect of the noise in the HQIR methodologies (fig. 2).

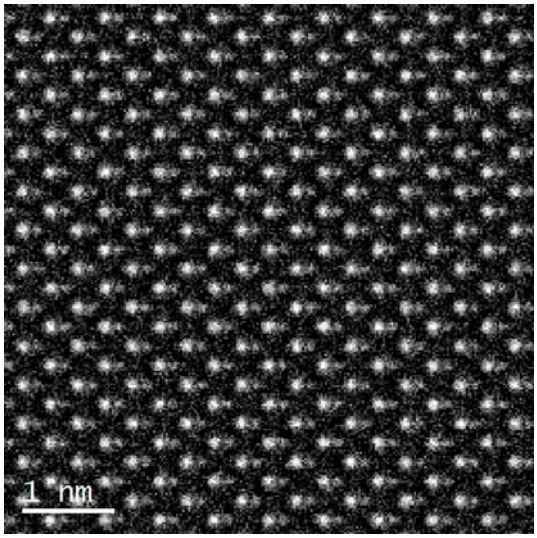

Fig.2. A 256x256 downsampled LR image obtained from the original simulation (fig. 1.) by adding noise (σ=0.02) and applying a downsampling by a factor of 4.

From these three high-resolution target images, three sequences of 10 LR images were generated through degradation procedures. These procedures involve the application of different displacements and rotations as well as a downsampling by a factor of 4. Gaussian zero-mean random variables are used for the shift (pixels) and rotation (degrees) parameters. For the shifts, a standard deviation of 4 pixels is used, while the rotation angles have a standard deviation of 0.0625 degrees. The sum of the displacements applied in the image series will be less than $lattice/2$, in the growth direction and less than $lattice/2\sqrt{2}$ in the x direction. In this way, we can guarantee that a dumbbell is aligned with its corresponding dumbbell from the other image and so we prevent an incorrect alignment with other dumbbell from the same row or column. Once the series of simulated LR images have been obtained, the experiment will focus on applying different registration and restoration methods in order to obtain a HQIR image that can be compared with the target high-resolution image.

The execution time and two quantitative/empirical measurements are used to assess the effects of these image enhancement algorithms on image quality. Indeed, Mean Absolute Error (MAE) can be used to assess the accuracy of the motion estimates (shift and rotation) and to evaluate detail accuracy and border

distortion. Secondly, Peak Signal to Noise Ratio (PSNR) will be applied to compare the original and the reconstructed image in terms of noise reduction.
MAE measures the amount by which the values of the original image differ from the HQIR image. It is calculated as the average of the absolute errors between the estimates, e_i, and the true values, y_i, used as reference:

$$MAE = \frac{1}{n}\sum |e_i - y_i| \quad (2)$$

PSNR, usually expressed in terms of the logarithmic decibel scale, is defined as the quotient between the maximum possible value of a signal (power) and the power of distorting noise that affects the quality of the representation[30]. The higher value of PSNR the higher quality of the image:

$$PSNR = 20log_{10}\left(\frac{MAX_f}{\sqrt{MSE}}\right) \quad (3)$$

where

- MAX_f is the maximum signal value that exists in the original image
- MSE is the Mean Squared Error:

$$MSE = \frac{1}{mn}\sum_{i=0}^{m-1}\sum_{j=0}^{n-1}\|f(i,j) - g(i,j)\|^2 \quad (4)$$

where

- *f* represents the matrix data of the original image
- *g* represents the matrix data of the degraded image in question
- *m* represents the numbers of rows of pixels of the images and i represents the index of that row
- *n* represents the number of columns of pixels of the image
- and *j* represents the index of that column

5. Results

5.1. Alignment

Five selected registration algorithms will be assessed: (1) Keren from the spatial domain, and (2) Marcel, (3) Lucchese, (4) Vandewalle and finally, (5) our proposal, Vandewalle variant using cross-correlation (Vandewalle_NCC), from the frequency domain approach. Table 2 summarizes the absolute errors estimates and computational time calculations. First and second columns refer to the particular registration approach for the three noise levels considered. Third and fourth columns show means and standard deviations of the rotation estimates, fifth and sixth columns show means and standard deviations (σ) of the motion estimates and last column refers to the computational time in seconds under the same hardware conditions.

In terms of rotation estimates, all the methods show very similar results for the three noise levels considered, with very low mean and standard deviation, except Lucchese approach, whose absolute error values are too high. However, when focusing on shift and time measurements there exist significant differences among the different approaches. The low computational time employed by Marcel and Lucchese methods does not compensate the poor results obtained by the shift estimate. For this reason, Lucchese and Marcel methods can be discarded to align HAADF images.

From the three remaining methods, the most accurate results are reached by our proposal, but at the cost of the highest computational time. Classical Vandewalle and Keren approaches show very similar results in terms of rotation and motion estimates, although the real-space based algorithm of Keren has the best results in terms of computational time.

Keren is a very good alternative when a trade-off between accuracy and computational time is required. However, our proposal of using Vandewalle_NCC clearly surpassed the accuracy of the rest of the algorithms, spending around thirty seven seconds, which results in a very insignificant awaiting time. Thus Vandewalle variant using cross-correlation is selected as the alignment approach to be applied hereafter.

5.2. Reconstruction

In this restoration stage, first, our procedure to choose the reference image has been implemented in order to reduce drift and border effects in the final HQIR image, and then the LR series have been registered applying Vandewalle_NCC. Then, 8 different reconstruction techniques from section 3 have been applied.

Figures 3 and 4 show as a scatter diagram of MAE/PSNR for each series degraded by noise using sigma values of 0.005, 0.001 and 0.02 against computational time values. LI and BI methods are simpler and the most computationally efficient. However, these approaches together with POCS, PG and IBP, have yielded to worse results in MAE as well as in PSNR in comparison to NLM approaches. HQIR images obtained by the application of both NLM methods show the less differences between the original and the HQIR intensity values (MAE) and have better quality, with the greatest PSNR values.

On the other hand, all the methods have the same behaviour against noise, showing worst MAE and PSNR results as the noise level increases. PG could be considered the most robust method against noise, since the differences between the 3 levels of noise are very low. At the highest noise level (0.02), results from PG and NLM tend to be more similar, although always NLM shows better accuracy and quality. Finally, in terms of the computational time, while LI or BI restoration only spends around 8 seconds, a NLM restoration uses 13 hours and NLM-median almost 24 hours. This awaiting time is compensated by the very accurate results that are achieved, namely, the lowest MAE and the

highest PSNR. PG algorithm could be an interesting option whenever the computing power is limited.

Table 2. Mean and standard deviation of the absolute error for rotations and shifts measurements as well as computational time in seconds of each registration algorithm when the series of images is degraded with different noise levels

Algorithm	Noise level	Rotation		Shifts		Time
		Mean	σ	Mean	σ	
Keren	**σ=0.005**	0,05º	0,04º	4,96 px	5,47 px	1,77 s
	σ=0.01	0,06º	0,04º	4,96 px	5,47 px	1,55 s
	σ=0.02	0,06º	0,04º	4,96 px	5,46 px	1,80 s
Marcel	**σ=0.005**	0,05º	0,03º	53,18 px	62,40 px	2,51 s
	σ=0.01	0,05º	0,03º	137,50 px	65,12 px	2,54 s
	σ=0.02	0,05º	0,03º	127,09 px	39,72 px	2,30 s
Lucchese	**σ=0.005**	58,81º	21,93º	111,57 px	69,05 px	2,73 s
	σ=0.01	56,31º	20,52º	135,41 px	58,07 px	2,76 s
	σ=0.02	64,94º	19,31º	107,98 px	56,79 px	2,40 s
Vandewalle	**σ=0.005**	0,08º	0,06º	5,66 px	3,59 px	6,06 s
	σ=0.01	0,09º	0,07º	4,43 px	2,90 px	5,84 s
	σ=0.02	0,06º	0,03º	4,66 px	2,87 px	5,38 s
Our proposal	**σ=0.005**	0,05º	0,03º	1,64 px	0,84 px	34,92 s
	σ=0.01	0,05º	0,03º	1,36 px	1,15 px	36,31 s
	σ=0.02	0,05º	0,03º	1,43 px	1,02 px	35,06 s

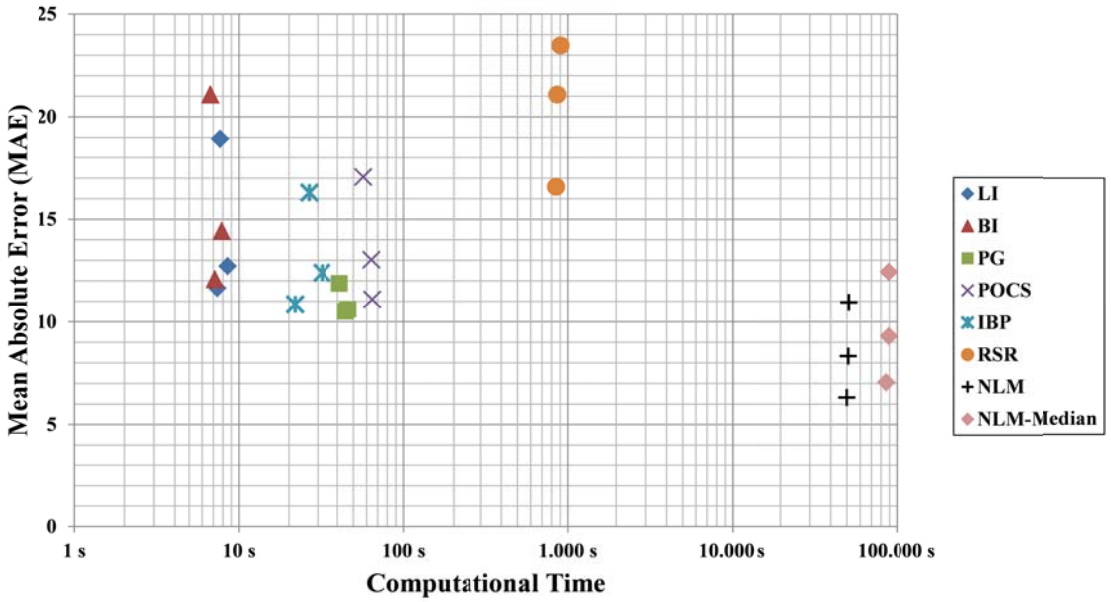

Fig. 3. Scatter diagram of MAE results for three noise levels of the different restoration methods (σ=0.005, 0.001, 0.02) against computational time.

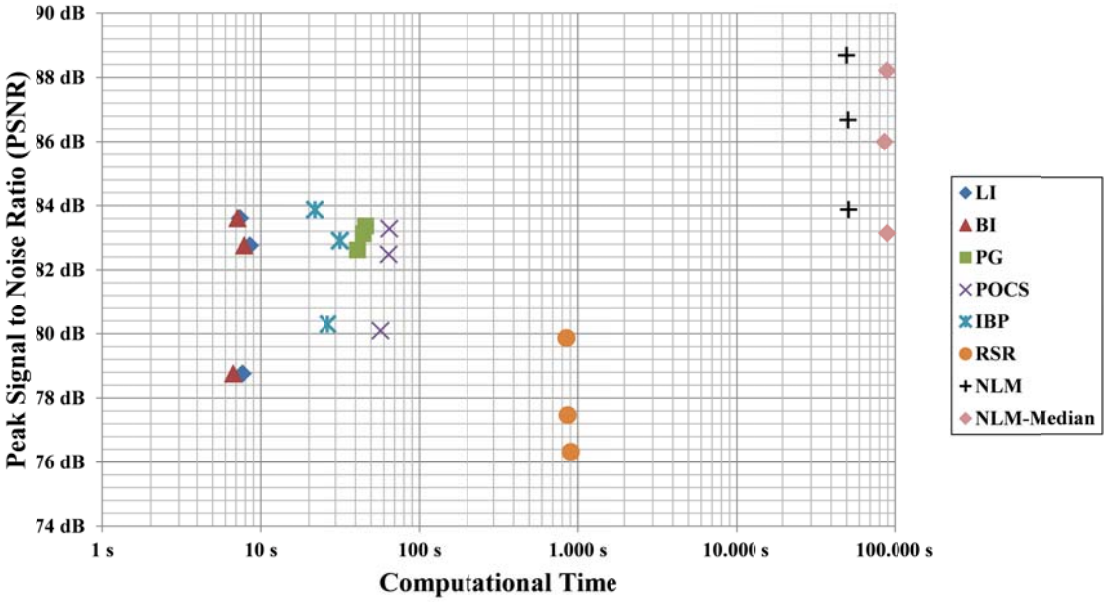

Fig. 4. Scatter diagram of PSNR values for three noise levels of the different restoration methods (σ=0.005, 0.001, 0.02) against computational time.

6. Practical experiment

In order to illustrate how the selected strategies for registration and restoration perform in real images, we have applied the proposed methodology to a series of experimental HRHAADF images. The sample consisted of a layer of InAs quantum dots (QDs) grown by molecular beam epitaxy (MBE) on a GaAs substrate. A series of 7 high-resolution aberration-corrected HAADF-STEM images with a size of 2048x2048 pixels were acquired at 200 kV along the [110] direction and captured every 8 seconds using a X-FEG FEI Titan probe-corrected STEM dedicated to advanced STEM imaging.

Fig. 5.a shows a frame from the experimental HAADF series, and fig. 5.b and fig. 5.c show the final HQIR image using PG and NLM algorithms respectively, calculated with double pixel density from this LR series. The zoomed-in area in fig. 5.a shows a raw noise at the background as well as parallel and vertical distortions to the scan direction that appear in the dumbbells of the experimental image. Qualitatively, it is clear that the atomic columns appear less blurred, where a reduction of the intensity of the background is noticed (zoomed-in areas in fig. 5.b and fig. 5.c). In addition, Fourier transform spots can be appreciated with enhanced clarity in the red (PG algorithm) and blue (NLM algorithm) profiles (fig. 5.e) traced on the transform (red box on fig. 5.d), while they are hardly visible in the experimental image (green profile). This significant increase of SNR can be appreciated tracing intensity line profiles through the experimental image (fig. 6.a) and the HQIR images (fig. 6.b and fig. 6.c), where an almost free-noise smoother signal and background can be appreciated in the HQIR images.

Following Bals et al. [31], the image precision could be defined as the standard deviation of anion-cation and anion-anion column distances. The atoms were fit

to the sum of 2, two-dimensional (2D) Gaussian functions to find the series-averaged atomic column positions on a zone in the substrate area (blue line).

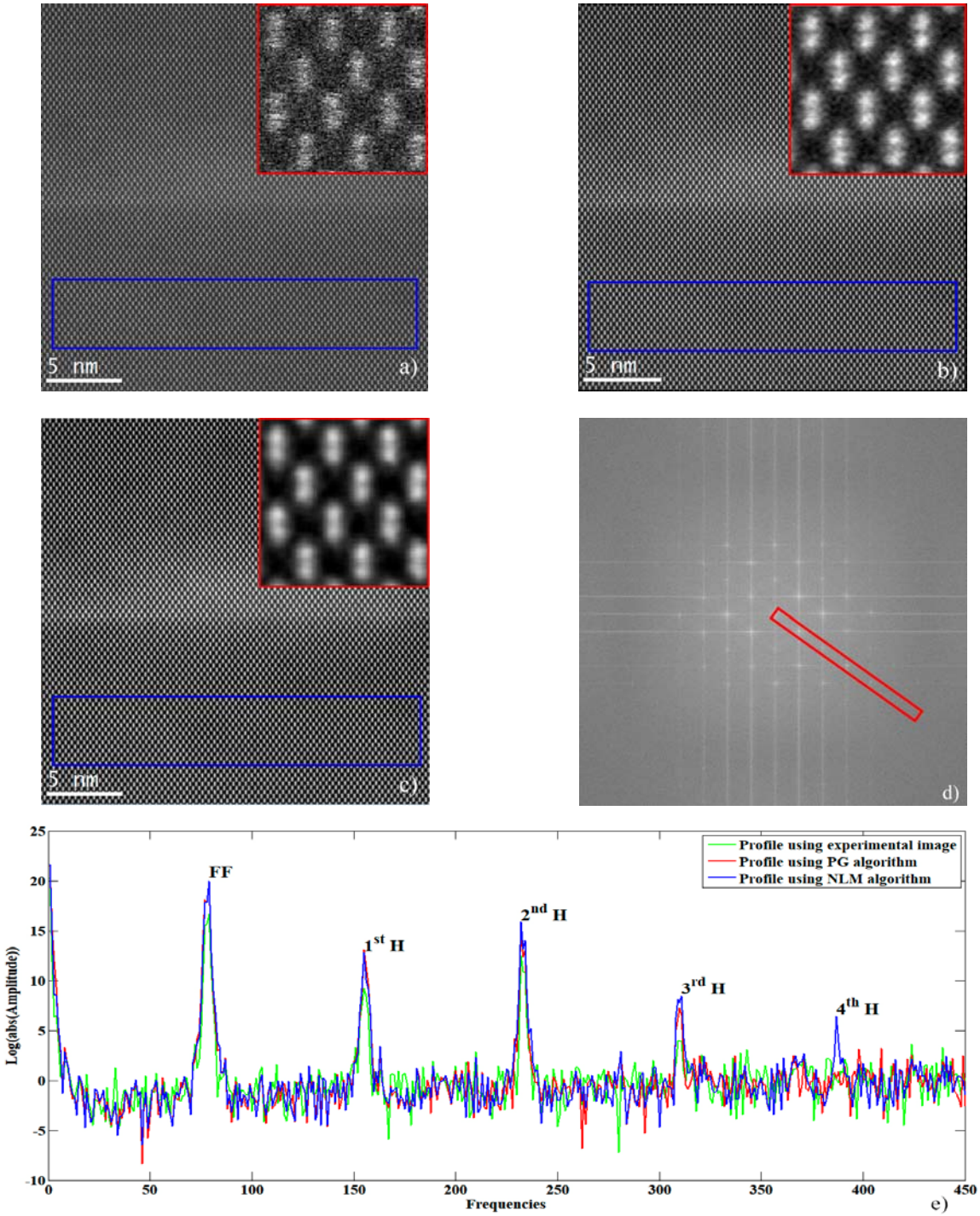

Fig. 5. (a) An experimental HAADF frame from the series of images of an InAs/GaAs QD and a subplot of a zoomed-in area. (b) HQIR images using PG algorithm. (c) HQIR images using NLM algorithm. (d) FFT of (c) with a red box that corresponds with the profile traced on the FFTs. (e) profiles using (green) experimental image, (red) PG algorithm and (blue) NLM algorithm. The spots are tagged as FF - Fundamental frequency, 1st H - First harmonic, 2nd H - Second harmonic, 3rd H - Third harmonic and 4th H - Fourth harmonic.

The results are shown in Table 3. Certainly, these results show how the precision has been improved in three to four times with regard to the low-resolution image, obtaining similar results to non-rigid approximations regarding

the standard deviation of the anion-cation distance and using only 7 images in the process.
Nevertheless, better results are obtained using NLM algorithm at the expense of a high computational time against PG approach. The NLM image can be used when high precision is needed, as in [32] where we demonstrate how HQIR can be used also to quantitative analysis, in particular how the precision of strain measurements can be enhanced in experimental images. Otherwise, PG methodology is appropriate to do the first evaluation of different experimental series in order to select the best series for a NLM restoration.

Table 3. Image precision using the standard deviation of anion vs cation and anion vs anion column separations proposed by Bals et al. The HQIR images improve the precision in three/four times with regard to the low resolution image using a zone in the substrate.

Reconstruction algorithms	$\sigma_{\text{anion-cation}}$	$\sigma_{\text{anion-anion}}$
Low resolution image	12,8 pm	7,8 pm
HQIR using PG algorithm	3,4 pm	1,9 pm
HQIR using NLM algorithm	3,4 pm	1,7 pm

7. Conclusions

In this paper, different frequency and spatial domains HQIR methods have been evaluated in the HAADF-STEM imaging field, differentiating between registration and restoration stages. For this comparison, simulated images have been used adding different distortions such noise, rotation and drift and finally this degraded images have been downsampled. In the case of the registration stage, a novel procedure to select the reference image has been implemented. This procedure guarantees the reduction of the global drift in the resulting HQIR image. Absolute error mean and standard deviation were used to assess 5 different alignment approaches. Among them, our proposal, a variant of the Vandewalle's approach using normalized cross-correlation, has obtained the best alignment results. MAE, PSNR and computational time have been used to compare the performance of eight restoration procedures. Papoulis-Gerchberg algorithm could be considered a good restoration method, since reasonable results can be obtained with little computational time. In contrast, the computational time in NLM is the highest, spending around half a day to get the final image. However, NLM has been selected as the best restoration approach to be applied to Z-contrast images because more accurate images, and with better quality, are achieved. To reduce this time, a parallel version could be implemented and run the software in supercomputers.
The HQIR methodology proposed in this work uses a simple rigid registration and addresses the most complex calculations in the reconstruction stage with

NLM. We have demonstrated that with a small number of experimental images resolution can be enhanced while distortions can be minimized, providing a more detailed and realistic HQIR image than any individual image from the series.

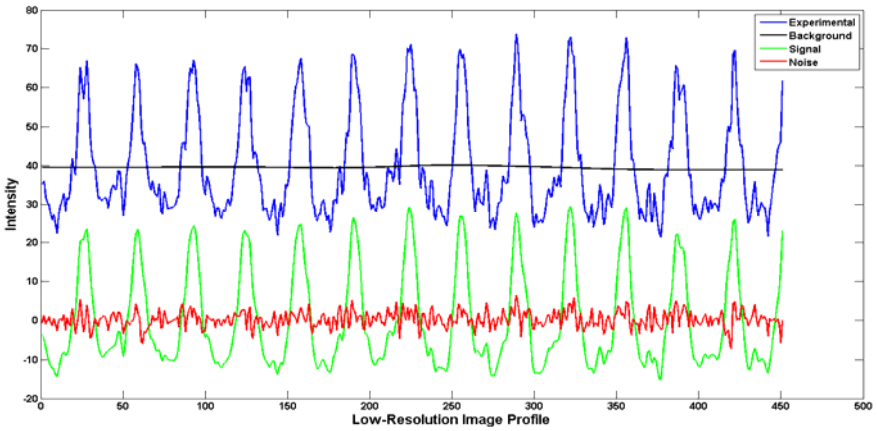

(a)

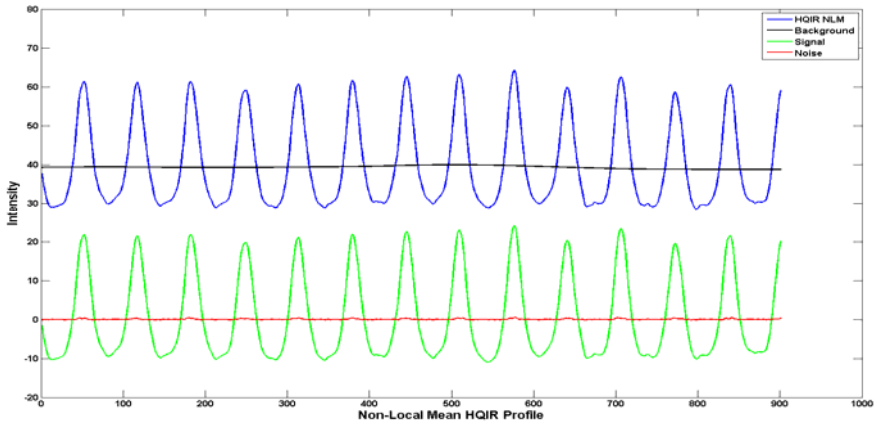

(b)

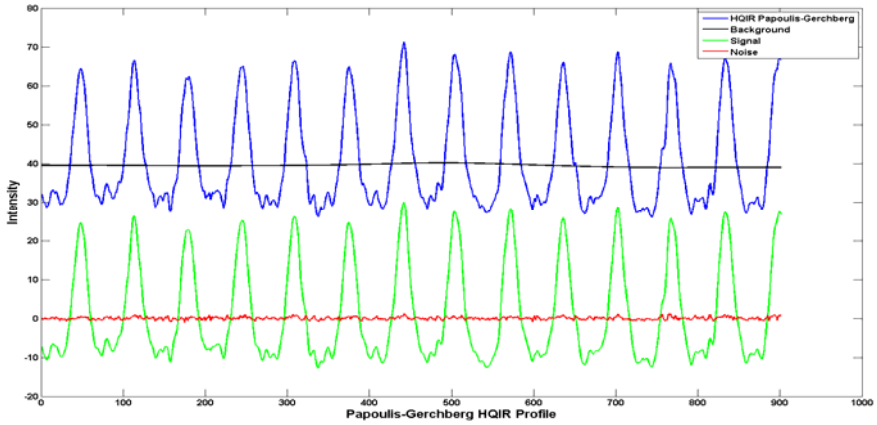

(c)

Fig. 6. (a) Line profiles of 450 pixels from the experimental image. (b) Line profile of 900 pixels from the HQIR image using PG restoration and (c) using NLM restoration. Each profile is decomposed into: background (black), noise (red), and the signal after subtraction of both, background and noise (green).

8. Acknowledgements

We would like to acknowledge funding from the European Union (project SEP-210135800), Spanish Government (projects MAT2013-47102-C2-1R, CTM2013-49796-EXP, TEC2014-53727-C2-2-R and CSD2009-00013), Junta de Andalucía Regional Government (project TEP3055/2012) and SCCYT-UCA for technical support.

9. References

[1] S. J. Pennycook and D. E. Jesson, “High-resolution Z-contrast imaging of crystals,” *Ultramicroscopy*, vol. 37, no. 1–4, pp. 14–38, 1991.

[2] P. D. Nellist and S. J. Pennycook, “The principles and interpretation of annular dark-field Z-contrast imaging,” *Adv. imaging electron Phys.*, vol. 113, pp. 147–203, 2000.

[3] V. Bannore, *Iterative-interpolation super-resolution image reconstruction: a computationally efficient technique*, vol. 195. Springer Science & Business Media, 2009.

[4] T. S. Huang, “Multi-frame image restoration and registration,” *Adv. Comput. Vis. Image Process.*, vol. 1, pp. 317–339, 1984.

[5] E. Betzig, G. H. Patterson, R. Sougrat, O. W. Lindwasser, S. Olenych, J. S. Bonifacino, M. W. Davidson, J. Lippincott-Schwartz, and H. F. Hess, “Imaging intracellular fluorescent proteins at nanometer resolution,” *Science (80-.).*, vol. 313, no. 5793, pp. 1642–1645, 2006.

[6] A. B. Yankovich, B. Berkels, W. Dahmen, P. Binev, S. I. Sanchez, S. A. Bradley, A. Li, I. Szlufarska, and P. M. Voyles, “Picometre-precision analysis of scanning transmission electron microscopy images of platinum nanocatalysts.,” *Nat. Commun.*, vol. 5, no. May, p. 4155, 2014.

[7] B. Berkels, P. Binev, D. Blom, W. Dahmen, R. Sharpley, and T. Vogt, “Optimized imaging using non-rigid registration,” *Ultramicroscopy*, vol. 138, pp. 46–56, 2014.

[8] B. Berkels, R. Sharpley, P. Binev, a Yankovich, F. Shi, P. Voyles, and W. Dahmen, “High Precision STEM Imaging by Non-Rigid Alignment and Averaging of a Series of Short Exposures,” *Microsc. Microanal.*, vol. 18, no. S2, pp. 300–301, 2012.

[9] B. Zitová and J. Flusser, “Image registration methods: A survey,” *Image Vis. Comput.*, vol. 21, no. 11, pp. 977–1000, 2003.

[10] L. Jones, H. Yang, T. J. Pennycook, M. S. J. Marshall, S. Van Aert, N. D. Browning, M. R. Castell, and P. D. Nellist, “Smart Align?a new tool for robust non-rigid registration of scanning microscope data,” *Adv. Struct. Chem. Imaging*, vol. 1, no. 1, p. 8, Dec. 2015.

[11] B. Marcel and M. Cattoen, “Edge and line detection in low level analysis,” in *Third Workshop on Electronic Control and Measuring Systems*, 1997, pp. 89–97.

[12] L. Lucchese and G. M. Cortelazzo, “A noise robust frequency domain technique for estimating planar roto-translation,” *IEEE Trans. Signal Process.*, vol. 48, no. 6, pp. 1769–1786, 2000.

[13] P. Vandewalle, S. Süsstrunk, and M. Vetterll, “A frequency domain approach to registration of aliased images with application to super-resolution,” *EURASIP J. Appl. Signal Processing*, vol. 2006, pp. 1–14,

2006.
[14] D. Keren, S. Peleg, and R. Brada, “Image sequence enhancement using sub-pixel displacements,” *Proc. CVPR ’88 Comput. Soc. Conf. Comput. Vis. Pattern Recognit.*, no. 3, pp. 742–746, 1988.
[15] R. S. Babu and K. E. S. Murthy, “A survey on the methods of super-resolution image reconstruction,” *Int. J. Comput. Appl*, vol. 15, no. 2, pp. 1–6, 2011.
[16] P. Viola and W. M. Wells III, “Alignment by maximization of mutual information,” *Int. J. Comput. Vis.*, vol. 24, no. 2, pp. 137–154, 1997.
[17] J. Yang and T. Huang, “Image super-resolution: Historical overview and future challenges,” *Super-resolution imaging*, pp. 3–25, 2010.
[18] S. Farsiu, D. Robinson, M. Elad, and P. Milanfar, “Fast and Robust Multi-Frame Super-Resolution,” *IEEE Trans. Image Process.*, vol. 13, no. 10, pp. 1327–1344, 2004.
[19] H. Stark and P. Oskoui, “High-resolution image recovery from image-plane arrays, using convex projections,” *J. Opt. Soc. Am. A*, vol. 6, no. 11, p. 1715, 1989.
[20] a. M. Tekalp, M. K. Ozkan, and M. I. Sezan, “High-resolution image reconstruction from lower-resolution imagesequences and space-varying image restoration,” *[Proceedings] ICASSP-92 1992 IEEE Int. Conf. Acoust. Speech, Signal Process.*, vol. 3, pp. 3–6, 1992.
[21] L. M. Bregman, “The relaxation method of finding the common point of convex sets and its application to the solution of problems in convex programming,” *USSR Comput. Math. Math. Phys.*, vol. 7, no. 3, pp. 200–217, 1967.
[22] A. Papoulis, “A new algorithm in spectral analysis and band limited extrapolation,” *IEEE Trans. Circuits Syst.*, vol. 22, no. 9, pp. 735–742, 1975.
[23] R. W. Gerchberg, “Super-resolution through error energy reduction,” *J. Mod. Opt.*, vol. 21, no. 9, pp. 709–720, 1974.
[24] M. Irani and S. Peleg, “Improving resolution by Image Registration,” *CVGIP Graph. Model. Image Process.*, vol. 53, no. 3, pp. 231–239, 1991.
[25] a. Buades and B. Coll, “A non-local algorithm for image denoising,” *Comput. Vis. Pattern*, vol. 2, no. 0, pp. 60–65, 2005.
[26] M. Protter, M. Elad, S. Member, H. Takeda, and S. Member, “Generalizing the Nonlocal-Means to Super-Resolution Reconstruction,” *IEEE Trans. Image Process.*, vol. 18, no. 1, pp. 36–51, 2009.
[27] P. Binev, F. Blanco-Silva, D. Blom, W. Dahmen, P. Lamby, R. Sharpley, and T. Vogt, “High Quality Image Formation by Nonlocal Means Applied to High-Angle Annular Darkfield Scanning Transmission Electron Microscopy (HAADF–STEM),” 2010.
[28] K. Nasrollahi and T. B. Moeslund, *Super-resolution: A comprehensive survey*, vol. 25, no. 6. 2014.
[29] J. Pizarro, P. L. Galindo, E. Guerrero, A. Yáñez, M. P. Guerrero, A. Rosenauer, D. L. Sales, and S. I. Molina, “Simulation of high angle annular dark field scanning transmission electron microscopy images of large nanostructures,” *Appl. Phys. Lett.*, vol. 93, no. 15, pp. 2006–2009, 2008.
[30] F. M. Candocia and J. C. Principe, “Super-resolution of images based on local correlations,” *IEEE Trans. Neural Networks*, vol. 10, no. 2, pp. 372–

380, 1999.
[31] S. Bals, S. Van Aert, G. Van Tendeloo, and D. Ávila-Brande, “Statistical estimation of atomic positions from exit wave reconstruction with a precision in the picometer range,” *Phys. Rev. Lett.*, vol. 96, no. 9, pp. 1–4, 2006.
[32] G. BÁRCENA-GONZÁLEZ, M. P. GUERRERO-LEBRERO, E. GUERRERO, D. FERNÁNDEZ-REYES, D. GONZÁLEZ, A. MAYORAL, A. D. UTRILLA, J. M. ULLOA, and P. L. GALINDO, “Strain mapping accuracy improvement using super-resolution techniques,” *J. Microsc.*, vol. 262, no. 1, pp. 50–58, Apr. 2016.